PAPER

Check for updates

Mechanocatalytic hydrogenolysis of benzyl phenyl ether over supported nickel catalysts†

Andrew W. Tricker, [ID] [ab] Sean Najmi, [ID] [a] Erin V. Phillips, [bc] Karoline L. Hebisch, [a] Jason X. Kang [ID] [a] and Carsten Sievers [ID] *[ab]

Mechanocatalysis is a promising approach for green, solvent-free biomass deconstruction and valorization. Here, the hydrogenolysis of benzyl phenyl ether (BPE), a model lignin ether, *via* ball milling is demonstrated over supported nickel catalysts at nominally room temperature and atmospheric hydrogen pressure. The hydrogenolysis reaction network closely follows that of solution-based reactions, with the primary products being toluene, phenol, and cyclohexanol. The mechanical energy during milling not only drives the chemical reactions but also activates the nickel by exposing fresh metallic surfaces from passivated particles, which replaces a thermal activation step. The hydrogenolysis rate is shown to be largely insensitive to the final nickel particle size, but reactivity of the oxide support can be enhanced during milling which contributes to carbon deposition. This work demonstrates the underlying chemistry necessary for mild lignin depolymerization using reductive mechanocatalysis.

Sustainability spotlight

The production of commodity chemicals and materials from alternative feedstocks is necessary to successfully transition from a fossil-based, linear economy to a sustainable, circular economy. The deconstruction and valorization of biomass, and lignin in particular, is a promising pathway to utilize renewable carbon. However, most conventional approaches rely on the use of organic solvents, which contribute a significant portion of the process-energy and can also have adverse effects on the environment. The current research demonstrates the feasibility of the underlying chemistry necessary to depolymerize lignin under solvent-free and ambient conditions. This work aligns with US SDG #12 (responsible consumption and production) by advancing an approach to utilize renewable resources while minimizing process waste production.

Introduction

As society shifts away from fossil-based fuels and chemicals, the necessity for complete utilization of biomass becomes ever more pressing. Lignin, a primary component of woody biomass, is an abundant renewable resource but is practically unutilized as a feedstock for chemicals and materials. Of the 60 million tonnes of lignin isolated annually, less than 2% is used for value-added products, while the rest is burned as a low value fuel.[1] Lignin is a heterogeneous, amorphous polymer that is primarily comprised of three propyl-phenolic monolignols (*p*-coumaryl alcohol, coniferyl alcohol, and sinapyl alcohol) linked together randomly by various C–O (β-O-4, α-O-4, 4-O-5) and C–C (β–β, β–5, 5–5) bonds.[2] However, the fractionation of lignin

from the lignocellulosic matrix typically changes the structure of the polymer and increases the abundance of condensed (C–C) linkages.[3] As the largest natural source of aromatic carbon, lignin is a promising, sustainable alternative starting point for historically benzene–toluene–xylene (BTX) derived chemicals if the polymer can be selectively depolymerized to mono-aromatics.

Two of the most promising approaches to depolymerize lignin utilize hydrogen as either a cleaving or stabilizing reagent: hydroprocessing and reductive catalytic fraction (RCF).[4] Hydroprocessing, generally performed with isolated lignin, combines hydrogenolysis of the linkages to produce monomers and hydrodeoxygenation (HDO) to upgrade monomers simultaneously.[5] These reactions tend to produce monomer yields between 10 and 20 wt%, with harsher reaction conditions increasing monomer yields at the expense of product selectivity.[4] RCF starts with complete lignocellulose and combines the isolation and depolymerization of lignin, where solvolysis formed monomers are stabilized before repolymerization can occur.[6] Most reported monomer yields from RCF studies range from 10 to 30 wt% for softwood and from 30 to 60 wt% for hardwood feedstocks with very high selectivities of phenolics. Both hydroprocessing and RFC reactions employed

[a]School of Chemical & Biomolecular Engineering, Georgia Institute of Technology, Atlanta, GA 30332, USA. E-mail: carsten.sievers@chbe.gatech.edu

[b]Renewable Bioproducts Institute, Georgia Institute of Technology, Atlanta, GA 30332, USA

[c]School of Chemistry and Biochemistry, Georgia Institute of Technology, Atlanta, GA 30332, USA

noble metals, such as Pt, Pd, Ru, or Rh, or transition metals, primarily Ni and Cu, on either acidic or neutral supports. These reactions often require elevated temperatures (130–450 °C), elevated hydrogen pressures (10–100 bar), and large quantities of organic solvents, such as methanol, dioxane, or THF.[4] The specialized equipment necessary for the combination of high hydrogen pressures and heated, flammable solvents, along with the energy demands for solvent recovery, currently stand as major barriers to scale up these processes.[7]

Mechanochemistry offers a novel approach for green chemical production by performing reactions under solvent-free conditions at nominally ambient temperatures and pressures.[8–10] The direct input of mechanical energy, such as collisions in a ball mill, can drive reactions between solid reactants and catalysts. This energy can influence the system in many ways, such as enhancing solid–solid mixing and contact,[11] creating fresh reactive surfaces,[12] forming localized thermal hot spots,[13] and altering reactivity of reagents[14] and catalysts.[15–17] The multitude of ways that mechanochemical reactions can occur has resulted in a broad range of applications, such as alloying,[12] pharmaceuticals[18] and absorbents[19] synthesis, consumer plastics deconstruction,[20,21] and waste recycling.[22]

Mechanical energy, without added chemicals or catalysts, has long been used as a method for pulping wood and pre-treating lignocellulose for conversion to fuels and chemicals.[23] In recent years, the use of mechanocatalysis for biomass valorization has seen a rise in popularity, albeit with an emphasis on cellulose or unfractionated lignocellulosic biomass.[24,25] Mechanocatalytic hydrolysis of cellulose and lignocellulose impregnated with HCl, H_2SO_4, or solid acids, such as delaminated kaolinite, can produce high yields of water-soluble sugar oligomers within a few hours of milling.[26–28] Additionally, the energy efficiency of the reaction has been shown to increase at least up to the kilogram scale while also maintaining greater than 90% yields of water-soluble oligosaccharides.[29] Studies on the degradation of isolated lignin have been more limited. Early work focused on the homolytic cleavage of model compounds during ball milling.[30,31] Mechanochemistry has since been utilized as a pretreatment method[32] or for alkaline[33,34] and oxidative[35] depolymerization. However, these approaches either rely on corrosive reactants (i.e., NaOH) or use a complex, multi-component mixture of homogeneous catalysts, which may be difficult to separate and recycle.

While the mechanocatalytic hydrogenation of benzene over nickel in a vibratory ball mill was reported as far back as 1963,[36] studies on reductive mechanocatalysis with gaseous hydrogen have been sparse.[37] The methanation of CO_2 over Ni/Fe/Ru on MgO catalysts[38] and LaNi alloys[39] and of CO over mixed FeCo and MgNi catalysts[40] have been demonstrated. The hydrogenation of numerous alkynes, alkenes, aromatics, and various functional groups have been reported using a feed of H_2 or splitting water in situ.[41–43] Recently, the reduction of N_2 to NH_3 with H_2 was reported using a batch planetary ball mill[44] and in continuous-flow vibratory ball mills.[16,45]

Herein, the mechanocatalytic hydrogenolysis of BPE was demonstrated under solvent-free, nominally ambient conditions (room temperature, 1 bar H_2) using supported nickel catalysts. Hydrogenolysis of model lignin ethers have been extensively studied under liquid phase conditions to glean insights into the underlying catalytic reactions and behavior of catalysts.[46–48] Benzyl phenyl ether (BPE) is studied here as a model compound for lignin because of the similarity in C–O bond strengths between BPE and the β-O-4 linkage in lignin.[49] Admittedly, BPE lacks the functional moieties of lignin (i.e., hydroxyl and methoxy groups), however the novelty and complexity of the interactions between the reagent, catalyst, and mechanical action necessitates a more simplified model system to draw meaningful insights. A process based on this approach would have a distinct advantage over traditional approaches by avoiding product-solvent separations.

Additionally, in this paper, the mechanocatalytic hydrogenolysis reaction network for BPE is elucidated. The in situ mechanical activation of the supported nickel catalysts, as well as recyclability and deactivation pathways, are investigated. Finally, the effects of the nickel support properties on the activity of the catalysts are probed. Insights gained on the catalytic system will aid in further developing processes for the solvent-free and mild depolymerization of lignin via reductive mechanocatalysis.

Experimental

Chemicals

Benzyl phenyl ether (BPE, 97%) and o-xylene (99%) were purchased from Alfa Aesar. Nickel on silica–alumina ($Ni_{53}SiAl$), silicon dioxide (quartz, ~99%), silica–alumina catalyst support (grade 135), nickel nitrate hexahydrate ($Ni(NO_3)_2 \cdot 6H_2O$, 99.999%), and guaiacol (>98%) were purchased from Sigma-Aldrich. Silica gel was purchased from Sorbent Technologies. Methanol (ACS grade) was purchased from VWR. Isopropyl alcohol (IPA, 99%, Lab Grade) was purchased from Ward's Science. Hydrogen (H_2, UHP, Grade 5) and nitrogen (N_2, UHP, Grade 5) were purchased from Airgas.

Catalyst synthesis

Three 5 wt% nickel catalysts were synthesized using amorphous silica–alumina ($Ni_{05}SiAl$), silica gel ($Ni_{05}Si_{high}$), and quartz ($Ni_{05}Si_{low}$). The catalysts were prepared by incipient wetness impregnation with an aqueous $Ni(NO_3)_2$ solution. The wetted samples were dried at 105 °C in air overnight. The dried samples were reduced in 7% H_2 in Ar at 450 °C (ramp from room temperature at 10 °C min^{-1}) for 8 h. The samples were exposed to and stored in air after returning to room temperature.

Catalyst characterization

Inductively coupled plasma-optical emission spectroscopy (ICP-OES). Acid digestion and inductively coupled plasma optical emission spectroscopy (ICP-OES) was performed by the Renewable Bioproducts Institute. Sample aliquot was weighed into a predigested beaker. The beaker with sample was placed on a hot plate. After 5 mL of concentrate nitric acid was added, the contents were reacted for 30 min under elevated

temperature (below boiling). This was followed by adding another 2.5 mL of concentrated HCl, and the mixture was reacted for another 30 min. The digested mixture was cooled to room temperature and was filtered through a grade 40 ashless Whatman filter paper. The filtering assemble was washed with de-ionized water and joined to the filtrate. The volume of the final aqueous solution was recorded. The ICP-OES instrument was periodically tested for performance, which includes detector calibration, align view and wavelength calibration. In each batch of sample analysis, the instrument was calibrated with standards for the target elements, and a four-point calibration curve was established for each interested element. The aqueous sample prepared as stated above was used for ICP-OES analysis.

N₂-physisorption. Nitrogen physisorption measurements were performed using a Micromeritics ASAP 2020 physisorption analyzer. The samples (50–100 mg) were evacuated at 50 °C and 10 μmHg for 1 min and subsequently degassed at 110 °C and 100 mmHg for 4 h prior to the measurement. The measurement was performed at 77 K. Surface areas were calculated based on the BET method for a p/p_0 range between 0.025 and 0.30.[50]

X-ray powder diffractometry (XRD). X-ray powder diffraction (XRD) patterns were obtained using an Empyrean diffractometer by Malvern Panalytical, which operates with CuKα radiation coming from a Bragg–BrentanoHD source with a wavelength of $\lambda = 1.5406$ Å. The mask was 4 mm, the divergence slit was fixed at $\frac{1}{4}°$, the anti-scatter slit was 1°, and the soller slits were 0.04 rad. With this optics, an area of 138.7 mm² of the sample was scanned. The generator was operating at a tension of 45 kV and a current of 40 mA. The sample stage was a reflection–transmission spinner, the detector was a PIXcel3D. Diffractograms were measured at incident angles from $2\theta = 15°$ to 100° with a step size of 0.0131303° and a number of steps of 6474. The time per step was set to 61.2 s, the scan speed was chosen to be 0.05471 s⁻¹. The sample was rotated during the measurement with a revolution time of 16.0 s. The detection limit was 0.5 wt%. Data analysis was performed using the HighScore Plus software by Panalytical.

Scanning transmission electron microscopy (STEM). The powder sample was dispersed in ethanol, then dropped on carbon coated Cu grids after ultrasonication for 5 min. A Hitachi HD2700 aberration-corrected scanning transmission electron microscope was used to record the high-angle annular dark-field (HAADF) STEM images. The electron beam convergent angle α was 27 mrad and the HAADF detector collection angle $\beta = 70$–370 mrad.

Raman spectroscopy. Visible Raman spectroscopy was performed on a Renishaw Raman spectrometer using an excitation wavelength of $\lambda = 488$ nm. The laser power was chosen between 1–10% of the total power (30 mW), the grating of the filter was 2400 lines per mm. Samples were analyzed with 50× magnification and an acquisition time between 5–20 s. The acquisition software was WiRE 5.2. The spectra were collected using a CCD detector. The acquired spectra were deconvoluted using the peak analyzer function of the OriginPro 2020 (V9.7) software.

Diffuse reflectance infrared Fourier transform spectroscopy (DRIFTS). DRIFTS spectra were collected using a Nicolet 8700

FT–IR equipped with a liquid nitrogen cooled MCT/A detector and the Praying Mantis (Harrick Scientific) accessory with a high temperature reactor for *in situ* studies. Spectra were averaged at 64 scans with a resolution of 4 cm⁻¹. All spectra were treated using the Thermo Scientific Omnic Software. A background of dried potassium bromide at 50 °C was used for all spectra. The sampling cup was filled with spent catalyst and then smoothed several times to ensure an even layer. The reactor was sealed and flushed with 100 sccm N₂ for 5 min to settle the sample bed. An initial spectrum of the pure milled catalyst was collected at 50 °C for spectral subtraction against the spent catalyst with species adsorbed. Spent catalysts were measured before at 50 °C and then ramped up to 700 °C at 10 °C min⁻¹, held for 30 min in 40 sccm N₂ and then cooled back down to 50 °C. All spectra were collected at 50 °C after the sample had been heated to 700 °C. Control experiments were conducted on unmilled $Ni_{05}Si_{high}$ and Ni05Si with physisorbed BPE. The catalyst was impregnated with BPE (dissolved in dichloromethane) *via* incipient wetness impregnation. DRIFTS spectra were collected for each control sample at 50 °C and after heating to 700 °C.

Mechanocatalytic reactions

Mechanocatalytic reactions were performed using a modified Retsch MM400 vibratory ball mill with a 25 mL stainless steel milling vessel. The milling vessel was modified to allow for continuous gas flow. The effluent line was heated to 160 °C and the effluent gas was bubbled through methanol (~10 mL with ~0.03 g o-xylene as an internal standard) cooled to 4 °C to trap volatile products leaving the reactor. Unless otherwise specified, reactions were conducted with 1.00 g of catalyst, 0.20 g of BPE, two 15 mm stainless steel grinding balls, and a milling frequency of 20 Hz in a continuous flow of H₂. The high catalyst to BPE ratio was necessary in order to keep the substrate a powder during milling. Due to the low melting point of BPE (40 °C), lower catalyst-to-reagent ratios resulted in liquefaction of the substrate and no observed reaction. This issue would not arise when milling polymeric materials, like lignin, and lower catalyst-to-reagent ratios can be used. Additionally, this type of system could be adapted to a continuous process at larger scales, allowing for more realistic reagent-to-catalyst ratios. The vessel was left unheated but milling induced an external temperature increase to ~30 °C within the reactor. The vessel was purged with N₂ for 15 min and then with H₂ for at least 15 min before milling began. After milling, the vessel was purged with N₂ for 1 h to remove additional residual volatile products.

Unconverted BPE and non-volatile products were measured after each reaction by removing the product-catalyst mixture from the milling vessel and sonicating in methanol (~10 mL) for 30 min. Roughly 90% of the sample mass could be recovered from the vessel. The remaining ~10% were left adsorbed on the vessel and balls or in the valve port of the ball mill. After sonication, o-xylene was added (~0.03 g) as an internal standard. The yield of volatile products over the course of the reaction was measured by taking aliquots (~0.05 mL) of the methanol trap.

Product yields were determined *via* gas chromatography using a Varian 450-GC with a fused silica column (Supelco, SPB-1, 60 m × 0.25 mm × 1.0 μm) and a flame ionization detector (FID). The GC-FID was equipped with a PolyArc reactor (Activated Research Company), which allowed for calibration-free quantification of the products.

The long-term stability of the $Ni_{53}SiAl$ catalyst was studied through a series of recycle experiments. The catalyst was milled for 2 h during the initial cycle and 4 h for the second and third cycles. After being washed with methanol to recover unconverted BPE and non-volatile products, the catalyst was vacuum filtered and dried under vacuum at room temperature. Similar to the mechanocatalytic reactions with the fresh catalyst, 1.00 g of the recycled catalyst was used. The same experimental procedures were used as the reaction with fresh catalyst. After vial transfers and filtration, only ∼65% of the spent catalyst mass could be recovered (∼0.65 g). So, spent catalyst samples of several different runs were combined for each recycle stage. For example, to produce enough sample to run a third cycle, two second cycle run were performed, which required four fresh catalyst runs.

Mechanocatalytic reaction kinetics

In order to semi-quantify the activity and the deactivation of the catalysts and the rate of carbon loss, the reaction is treated as a simplified system with only two first order reactions. The first is the hydrogenolysis of BPE to toluene and the second is the coke formation from BPE. Since the toluene yield is based on products detected in the condenser, it is assumed that all the produced toluene is found in the condenser and that toluene does not participate in the coking reaction. Initially, the mechanocatalytic hydrogenolysis reactions were fit using this simplified kinetic model (eqn (1)–(4)), where X_{BPE} is the conversion of BPE, k_H is the hydrogenolysis rate constant, m_{Ni} is the mass of nickel, k_C is the coking rate constant, and Y_{tol} is the yield of toluene in the condenser. Eqn (3) and (4) are the analytical solutions to the integration of eqn (1) and (2), respectively. Since X_{BPE} was measured for several time points for fresh $Ni_{53}SiAl$, eqn (3) was fit to solve for $k_H \cdot m_{Ni} + k_C$.

$$\frac{dX_{BPE}}{dt} = -(k_H(t) \cdot m_{Ni} + k_C)(1 - X_{BPE}(t)) \tag{1}$$

$$\frac{dY_{tol}}{dt} = k_H(t) \cdot m_{Ni} \cdot (1 - X_{BPE}(t)) \tag{2}$$

$$X_{BPE}(t) = 1 - \exp(-(k_H \cdot m_{Ni} + k_C)t) \tag{3}$$

$$Y_{tol}(t) = \frac{k_H \cdot m_{Ni}}{k_H \cdot m_{Ni} + k_C}(1 - \exp(-(k_H \cdot m_{Ni} + k_C)t)) \tag{4}$$

For experiments where the full product yields were only measured once and the conversion of BPE was incomplete, $k_H \cdot m_{Ni} + k_C$ were be determined by eqn (3) to yield eqn (5) and using the final conversion. k_H was fit using Solver in Excel to minimize the error between the model and the toluene yield from the condenser. Due to the observed induction period in

the condenser yield, a delay term was also fit. For $Ni_{53}SiAl$-cycle 2, which was run only once and had nearly 100% conversion of BPE, calculating k_C from eqn (5) would have resulted in high uncertainty and was instead approximated with the k_C of Ni_{53}-SiAl-cycle 3.

$$k_H \cdot m_{Ni} + k_c = -\frac{\ln(1 - X_{BPE}(t_{final}))}{t_{final}} \tag{5}$$

To assess the deactivation of $Ni_{53}SiAl$, a first-order deactivation term was included in the model (eqn (6)), where k_D is the deactivation rate constant. No analytical solution to eqn (S1), (S2), and (S6)† exists, so the equations were fit numerically. A Matlab script based on the built-in functions fmincon (error minimization) and ode45 (differential equation solver) was used to determine k_D and the initial hydrogenolysis rate constant ($k_{H,0}$). An average k_C was used and assumed constant.

$$\frac{dk_H}{dt} = -k_D \cdot k_H(t) \tag{6}$$

Results and discussion

Catalyst characterization

Inductively coupled plasma optical emission spectroscopy (ICP-OES) analysis of the nickel loadings of the catalysts showed that the commercial nickel on silica–alumina ($Ni_{53}SiAl$) sample contained 53.4 wt% Ni, while the synthesized Ni catalysts with silica–alumina, high surface area silica and low surface area silica ($Ni_{05}SiAl$, $Ni_{05}Si_{high}$, and $Ni_{05}Si_{low}$) had 4.42 wt%, 4.93 wt%, and 4.85 wt% Ni, respectively. The BET surface areas of $Ni_{53}SiAl$, $Ni_{05}SiAl$, $Ni_{05}Si_{high}$, and $Ni_{05}Si_{low}$ were 85.3 $m^2 g^{-1}$, 499 $m^2 g^{-1}$, 515 $m^2 g^{-1}$, and 6.7 $m^2 g^{-1}$, respectively. Adsorption and desorption isotherms are shown in Fig. S1.† X-ray powder diffractometry (XRD) of $Ni_{53}SiAl$ showed the presence of both Ni and NiO, while only peaks corresponding to metallic Ni were observed in the diffractograms of $Ni_{05}SiAl$, $Ni_{05}Si_{high}$, and $Ni_{05}Si_{low}$ (Fig. S2†). Scanning transmission electron microscope (STEM) images showed that the nickel particles of $Ni_{53}SiAl$ were encapsulated in NiO (Fig. 1a). Similarly, STEM showed outer layers of NiO on the nickel particles for $Ni_{05}SiAl$, $Ni_{05}Si_{high}$, and $Ni_{05}Si_{low}$ (Fig. 1b–d). Energy dispersive spectrometry (EDS) mapping of $Ni_{53}SiAl$ showed particles uniformly coated in nickel (Fig. 1e), while the low nickel loading catalysts had discrete nickel particles (Fig. 1f–h). $Ni_{05}SiAl$, $Ni_{05}Si_{high}$, and $Ni_{05}Si_{low}$ had initial particle sizes of 18.7 nm, 15.1 nm, and 46.7 nm, respectively (Fig. S4†). The high abundance of nickel on $Ni_{53}SiAl$ prevented the measurement of enough particles to determine initial particle size.

Hydrogenolysis reaction network

The mechanocatalytic reactions were conducted in a vibratory ball mill (Retsch, MM400) reactor, modified to allow for the continuous flow of H_2 (Scheme 1). The catalyst and BPE were placed together in the milling vessel without additional pretreatment. While the vessel was not externally heated or
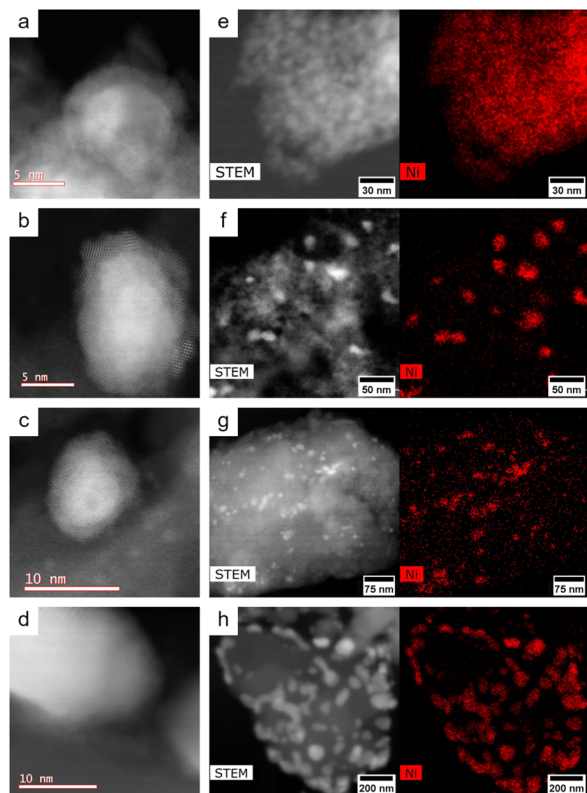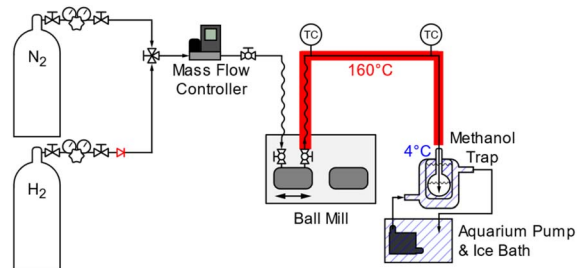
Fig. 1 STEM images of individual nickel particles on (a) Ni$_{53}$SiAl, (b) Ni$_{05}$SiAl, (c) Ni$_{05}$Si$_{high}$, and (d) Ni$_{05}$Si$_{low}$. STEM images and EDS mapping of nickel for whole catalyst particles of (e) Ni$_{53}$SiAl, (f) Ni$_{05}$SiAl, (g) Ni$_{05}$Si$_{high}$, and (h) Ni$_{05}$Si$_{low}$.

Scheme 1 Depiction of the flow-through ball mill reactor.

pressurized, the milling caused the external vessel temperature to rise slightly to ∼30 °C. The reactor effluent was bubbled through methanol cooled to 4 °C to collect volatile products, and the methanol solution was sampled periodically to determine the yield of toluene during milling as a proxy for the extent of reaction. Gas chromatography was used to quantify products collected in the methanol trap and washed off the catalyst after reaction. The majority of the hydrocarbon products (toluene, benzene, cyclohexane) were recovered in the methanol trap, while oxygenated products (phenol, cyclohexanol) remained in the milling vessel and were collected from the catalyst wash.

Analysis of reaction products formed over a commercial 53 wt% nickel on silica–alumina (Ni$_{53}$SiAl) catalyst after various milling times elucidated the mechanocatalytic reaction network of benzyl phenyl ether (BPE), which closely follows reported pathways during thermally catalyzed reactions (Fig. 2).[49,51–54] At early milling times, the main products were toluene (**1a**) and phenol (**1b**), which are formed by hydrogenolysis of the benzyl ether bond. Benzyl alcohol (**8**) was not detected, which is unsurprising since the bond dissociation energy of the benzyl ether bond (56.4 kJ mol^{-1})[55] is much lower than that of the phenyl ether bond (95.7 kJ mol^{-1}).[56] Yields of hydrogenated ethers (**4** & **5**) passed through maxima (∼1%) at 60 min, suggesting that hydrogenolysis of these compounds occurred, but did not significantly contribute to the formation of the single-ring products. The formation of methyl cyclohexane (**2**) and cyclohexanol (**3**) predominantly occurred through the hydrogenation of toluene and phenol, respectively. Phenol hydrogenation to cyclohexanol was established as a reaction path based on the maximum in the phenol yield after 60 min. Low methyl-cyclohexane yields (<1%) can be explained by the removal of toluene vapors from the reactor prior to be being hydrogenated or a lower affinity of toluene to the active sites for hydrogenation reactions on the catalyst. Benzene (**6**) and cyclohexane (**7**) were detected after 60 min and 120 min, respectively. Their formation is attributed to hydrodeoxygenation of phenol and cyclohexanol. Since benzene and cyclohexane were only found in the condenser, benzene is expected to volatilize before hydrogenation can occur. Alkylation reactions and heavier products have been reported in thermocatalytic systems.[52,57,58] The decreasing carbon balance with increasing milling time could be attributed to the formation of similar species. Over the course of the reaction, the yield of toluene consistently exceeds the combined yields of phenol and cyclohexanol, meaning the adsorption of phenolates on the catalyst surface is another source of carbon loss. Overall, the nickel catalyst behaves similarly in mechanochemical and thermochemical systems. Thus, it may be possible to extrapolate the results of other thermocatalytic reactions to predict the performance of mechanocatalytic processes for lignin conversion.

A series of experiments was conducted to explore the catalytic transfer hydrogenolysis[59,60] of BPE using isopropanol (IPA) in place of H$_2$ (ESI Section S2.2†). IPA was added to the milling vessel (125 μL) and the reaction was conducted in a continuous flow of N$_2$. Here, a 2.4% yield of toluene and a 1.6% yield of phenol was measured after 180 min. In principle, IPA can work as a hydrogen transfer agent for mechanocatalytic hydrogenolysis, but additional optimization and study would be necessary.

Mechanocatalyst activation

Before traditional thermocatalytic reactions, nickel must typically be reduced *in situ* at elevated temperatures (*i.e.*, activated) to remove passivating oxide layers or reduce nickel oxide particles to the metal altogether. Here, thermal pretreatment of the passivated nickel catalysts was not necessary as milling in a reductive environment activated the catalyst. Initially, the nickel particles of the Ni$_{53}$SiAl catalyst were encapsulated by a layer of NiO (Fig. 3a–c). However, thermally oxidized Ni$_{53}$SiAl
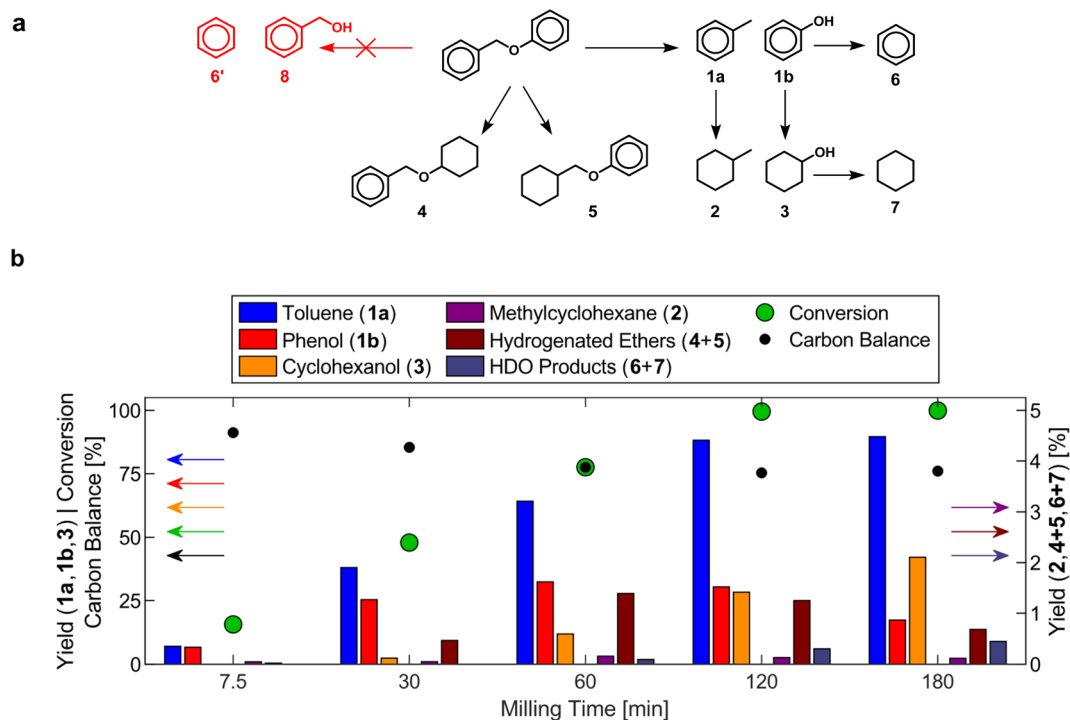
Fig. 2 (a) Reaction network during the mechanocatalytic hydrogenolysis of BPE. (b) Product yields, conversion of BPE, and carbon balance during the mechanocatalytic hydrogenolysis of BPE with $Ni_{53}SiAl$. 1.00 g $Ni_{53}SiAl$, 0.20 g BPE, 25 mL S. S. vessel, 2 × 15 mm S. S. grinding balls, 20 Hz, 60 sccm H_2. Numerical values are reported in Table S1.†

(Fig. S4†) showed significantly less activity (Fig. 3d). Attrition during milling is expected to remove the nickel oxide layer, liberating the active metallic nickel. Particularly when milling hard and brittle material, localized hot spots haven been shown to form[13] which may produce temperatures high enough to directly reduce the NiO to metallic Ni in the presence of H_2. The mechanochemical reduction of the NiO could explain why the rate of toluene production increased during milling with the oxidized $Ni_{53}SiAl$. Importantly, the potential local thermal energy is not sufficient to break the BPE ether bond homolytically. Control experiments were conducted with BPE milled with $Ni_{53}SiAl$ in N_2 and milled with just silica–alumina in H_2, and no conversion was detected in either case. Thus, mechanical energy both drives the hydrogenolysis reaction and activates the catalyst, removing the need for high temperature pretreatments and allowing for a fully ambient system.

Catalyst recycling and deactivation

The accumulation of toluene in the condenser allows for determining a lower limit of the hydrogenolysis rate. The toluene yield profile in the condenser during milling with fresh $Ni_{53}SiAl$ for 120 min (Fig. 4a – cycle 1) closely matched the progression of the toluene yield during the full product analysis (Fig. 2b). An induction period for toluene accumulation in the condenser of about 10 min was observed, which could be attributed to a catalyst activation period. However, at 7.5 min, the full toluene yield was 7% (compared to just 1% for the condenser toluene yield), suggesting the delay is an artifact of

the reactor system rather than, for example, a period needed to mechanically activate the nickel.

To evaluate the longer-term stability of the catalyst under such intense conditions, the $Ni_{53}SiAl$ catalyst was recycled twice. After each reaction, the catalyst was washed with methanol to analyze the complete product profile, and then filtered and dried under vacuum overnight at room temperature. The toluene yields for each cycle (Fig. 4a) showed continuous deactivation of the catalyst. In the second cycle, the toluene yield flattened after three hours of milling, trending toward a maximum toluene yield of 65%. During the third cycle, the toluene yield increased over the whole 4 h experiment, but only a 30% yield was achieved. Similar to the first cycle, an induction period of about 10 min was observed in the second and third cycle. As expected from the toluene yield profiles, the full product profiles showed nearly 100% conversion of BPE by the end of cycle 2 and incomplete conversion (65%) by the end of cycle 3 (Fig. 4b). Deactivation of the nickel was also observed in the decreased selectivity of cyclohexanol to phenol between cycle 2 (69%) and cycle 3 (45%). Finally, significant carbon loss was observed for each cycle.

The carbon balance suggests carbonaceous deposits form as undesired side reactions with increasing milling time. Raman spectroscopy was performed on the spent catalyst after each cycle to qualitatively detect coke deposits (Fig. 4c). Three bands in the Raman spectra of spent catalysts were detected: the G-band (1580 cm^{-1}; ideal graphitic lattice vibrations), the D_1-band (1350 cm^{-1}; vibrations of graphene layer edges), and the D_2-band (1610 cm^{-1}; surface graphene layers). These three
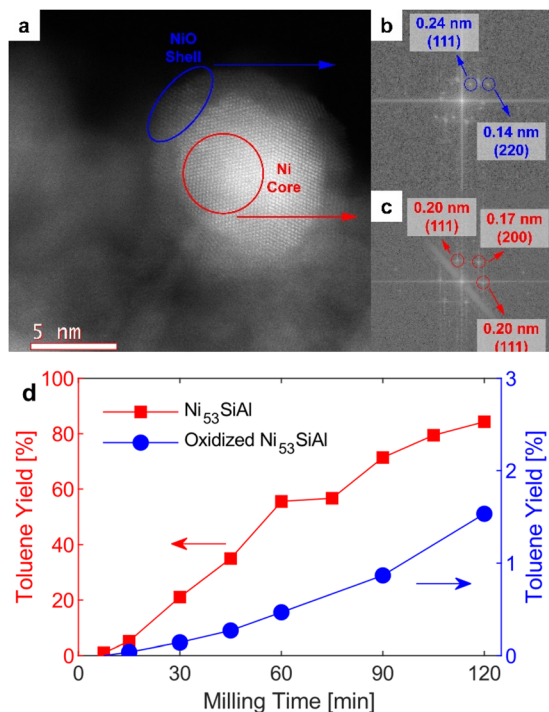
Fig. 3 (a) STEM image of a nickel particle from $Ni_{53}SiAl$ showing a NiO shell around a Ni core. Fourier transformation of a region of (b) the shell (blue ellipse) and (c) the core (red circle) showing d-spacings corresponding to NiO and Ni, respectively. (d) Yields of toluene in the condenser during mechanocatalytic hydrogenolysis of BPE over $Ni_{53}SiAl$ (red squares) and thermally oxidized $Ni_{53}SiAl$ (blue circles). 1.00 g catalyst, 0.20 g BPE, 25 mL S. S. vessel, 2×15 mm S. S. grinding balls, 20 Hz, 60 sccm H_2.

bands are indicative of polyaromatic coke.[61] At longer milling times, the relative intensity of the D-bands increased (compared to the G-band), which is supported by deconvolution and fitting of the bands (Table S2†). This increase of the D-bands and the decrease of the G-band suggest that the coke transformed to a more disordered and amorphous structure, which is expected with extended milling times.[62] Additional changes to the catalyst between cycles were investigated as well. Agglomeration of nickel particles was not observed in STEM-EDS images of the spent catalysts (Fig. S6†) and no loss of nickel was detected between cycles (Fig. S7†). Additionally, significant oxidation of the nickel, due to handling in air, was not observed in XRD between each cycle (Fig. S8†), although this does not rule out the formation of amorphous oxide phases. These results suggest that the deactivation occurs predominantly through the formation of adsorbed phenolates, which further react to form polyaromatic coke, resulting in blockage of active sites rather than mechanical degradation of the catalyst due to milling.

Phenolates and catecholates are well known to strongly bind to catalysts,[63] so the higher functionality of lignin is expected to exacerbate the formation of carbon deposits. The HDO of guaiacol, a more functionalized model compound, was briefly studied (ESI Section S4†). After 180 min, catechol, phenol, and cyclohexanol were detected at similar yields as HDO products during the hydrogenolysis of BPE (<1%), while the carbon

balance was slightly lower (62% compared to 77%). Future work will focus on adapting reaction engineering strategies, such as simultaneous hydrolysis,[64] to desorb phenolates or the use of redox active catalysts,[65,66] to recover adsorbed products and prevent further side reactions.

Generally, the energy dose is a key descriptor for mechanochemical kinetics.[21,67] However, the mechanochemical conditions were not varied in this study, so a simplified kinetic model is suitable here to provide a more quantitative description of the catalyst activity and deactivation. The system was approximated by two reactions: hydrogenolysis of BPE (k_H) and deposit formation (k_C), both first order with respect to BPE (eqn (1)–(5)). Initially, the conversion of BPE and yield of toluene for each cycle were fit independently to determine k_H and k_C (Fig. S5†). Both cycle 1 and cycle 3 had similar rates of coke formation ($k_{C,1}$ = 0.17 h^{-1}; $k_{C,3}$ = 0.16 h^{-1}), suggesting the activity of the catalyst toward coke formation is constant across all three cycles. Due to the high final conversion in cycle 2, calculating $k_{C,2}$ directly would result in high uncertainty. Thus, the value for $k_{C,3}$ was used during the fitting. The results of this kinetic model confirm the deactivation of the catalyst toward hydrogenolysis with a decrease in the rate constant between each cycle ($k_{H,1}$ = 2.0 h^{-1} g_{Ni}^{-1}; $k_{H,2}$ = 0.89 h^{-1} g_{Ni}^{-1}; $k_{H,3}$ = 0.20 h^{-1} g_{Ni}^{-1}). By the third cycle, the catalyst retained only a tenth of its initial activity. Next, all three cycles were fit simultaneously, using an average k_C of 0.163 h^{-1}, with a first order deactivation term introduced to the hydrogenolysis rate constant (eqn (6)). These fits were overlaid on the toluene yields in Fig. 5a. This fit shows an initial rate constant ($k_{H,0}$) of 2.5 h^{-1} g_{Ni}^{-1} and that the catalyst deactivated at a rate of 34% per hour of milling (k_D = 0.34 h^{-1}). The good agreement between the observed activity of the catalyst and the deactivation model suggests a continuous mechanism is occurring during milling instead of discrete deactivation occurring between cycles.

Influence of catalyst support

To explore the influence of the support properties on the reactivity, three catalysts with 5 wt% nickel loadings were synthesized using varying supports: a high surface area silica–alumina (499 m^2 g^{-1}, $Ni_{05}SiAl$), high surface area silica (515 m^2 g^{-1}, $Ni_{05}Si_{high}$), and low surface area silica (6.7 m^2 g^{-1}, $Ni_{05}Si_{low}$). BPE hydrogenolysis was performed for 180 min with each catalyst. The yield of toluene over the course of the reaction (Fig. 5a) showed a constant increase for $Ni_{05}Si_{low}$, while the rate of toluene formation diminished with time for $Ni_{05}SiAl$ and $Ni_{05}Si_{high}$. The simplified kinetic model (eqn (4) and (5)) was applied to these reactions to determine the hydrogenolysis rate constant (fits shown in Fig. 5a). $Ni_{05}SiAl$ (k_H = 0.81 h^{-1} g_{Ni}^{-1}) and $Ni_{05}Si_{low}$ (k_H = 0.83 h^{-1} g_{Ni}^{-1}) had similar hydrogenolysis rates, which were approximately 33% lower than the rate of $Ni_{05}Si_{high}$ (k_H = 1.21 h^{-1} g_{Ni}^{-1}). The nickel particle size had a weak correlation with the activity of the catalyst. Nickel particles observed using STEM-EDS on $Ni_{05}SiAl$ and $Ni_{05}Si_{low}$ agglomerated during milling to a size on the order of 100 nm (Fig. S9†), while the size of the nickel particles on $Ni_{05}Si_{high}$ (15.1 nm) did not appreciably change over the course of the
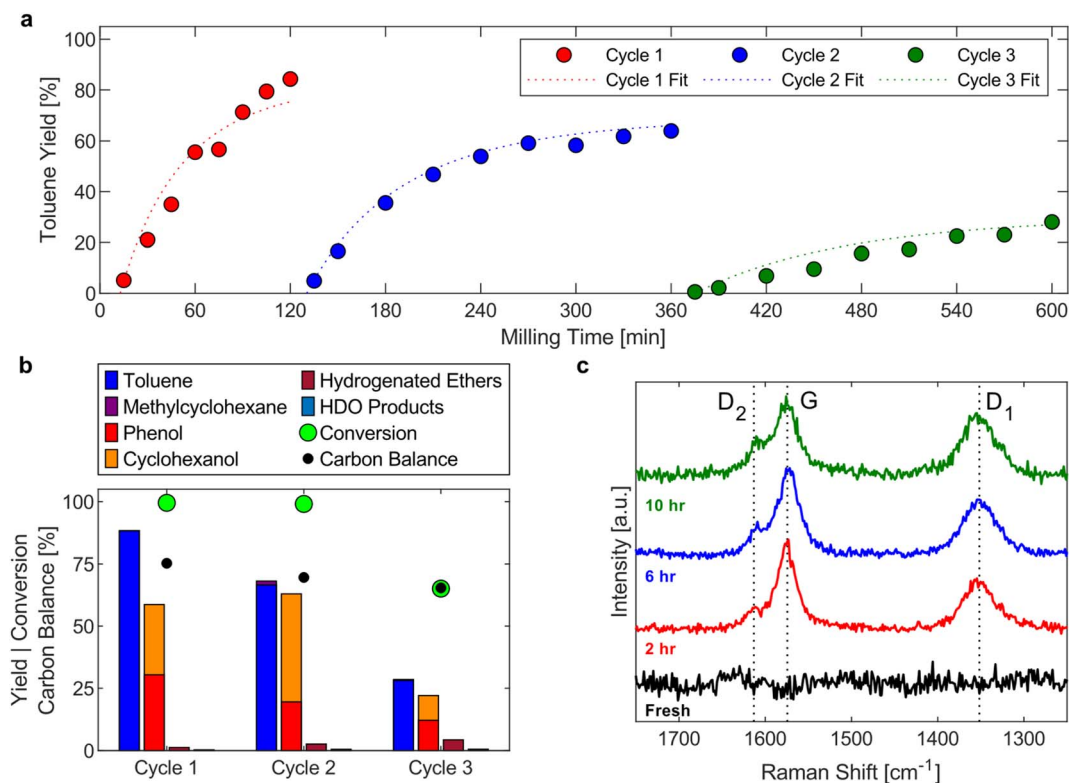
Fig. 4 (a) Toluene yield in the condenser during the hydrogenolysis of BPE with fresh $Ni_{53}SiAl$ (cycle 1) and recycled $Ni_{53}SiAl$ (cycle 2 and cycle 3). Fits from the kinetic modelling are overlaid the toluene yields. (b) Full product yields, conversion of BPE, and carbon balance after the hydrogenolysis reaction of BPE with fresh and recycled $Ni_{53}SiAl$. 1.00 g $Ni_{53}SiAl$, 0.20 g BPE, 25 mL S. S. vessel, 2 × 15 mm S. S. grinding balls, 20 Hz, 60 sccm H_2. (c) Raman spectra of fresh $Ni_{53}SiAl$ (black), $Ni_{53}SiAl$ after 2 h of reaction (after cycle 1) (red), $Ni_{53}SiAl$ after 6 h of reaction (after cycle 2) (blue), and $Ni_{53}SiAl$ after 10 h of reaction (after cycle 3) (green).

reaction. The reduction of the accessible nickel surface area by roughly one order of magnitude only corresponded to a 33% lower rate constant. This resistance to deactivation from agglomeration could have several explanations. The agglomeration may be indicative of more effective mechanical activation of nickel particles or larger nickel particles may more efficiently convert mechanical energy into chemical energy. The pores of the high surface area supports can also allow for nickel particles to be effectively shielded from direct mechanical forces. However, the similarity in the rate constants for the three catalysts suggests porosity does not significantly influence mechanical activation.

While the hydrogenolysis rates were similar among the three catalysts, the production of undesirable side products was much higher on the high surface area catalysts. Reactions with either $Ni_{05}SiAl$ or $Ni_{05}Si_{high}$ resulted in carbon balances of just 30%, while the reaction with $Ni_{05}Si_{low}$ had a carbon balance of 82% (Fig. 5b). The three spent catalysts were analyzed with Raman spectroscopy to determine the nature of the carbon deposits (Fig. 5c). Spent $Ni_{05}SiAl$ exhibited the same characteristic bands for polyaromatic coke as the spent $Ni_{53}SiAl$ (Fig. 4c). The spectrum of spent $Ni_{05}Si_{high}$ did not show polyaromatic coke, despite a similar deficit in the carbon balance. Only a single band at 1596 cm^{-1} was observed in the two spent silica supported catalysts, suggesting that the deposits are

predominantly mono-aromatic species.[68,69] The deposits on $Ni_{05}Si_{high}$ and $Ni_{05}Si_{low}$ were further analyzed using *in situ* DRIFTS (Fig. 5d). The region between 1400 and 1600 cm^{-1} corresponds to ring vibrations of aromatic species.[70] After heating the samples to 700 °C, the presence of aromatics remaining on the $Ni_{05}Si_{high}$ catalyst was much greater than the residue on the $Ni_{05}Si_{low}$ or nonmilled $Ni_{05}Si_{high}$ impregnated with BPE (Fig. S10†). This indicates chemisorption or encapsulation of the remaining aromatic species onto the $Ni_{05}Si_{high}$ surface.

The higher surface area of the support is most likely responsible for the discrepancy in carbon balances, as opposed to catalytic activity for undesirable side reactions. As a result of milling, the Si–O bonds can break and create transient, reactive sites.[71–73] Due to a larger abundance of surface Si–O bonds in the high surface area support, it is plausible that ruptures result in more reactive sites compared to the low surface area support. The higher density of active sites from rupturing can thus be responsible for more adsorbed species and a lower carbon balance on the $Ni_{05}Si_{high}$. Additionally, mechanochemical conditions could transform the catalyst in a way that leaves carbonaceous materials encapsulated in closed pores. A similar mechanism is expected to occur with $Ni_{05}SiAl$, but with the inherent acid sites of the silica–alumina also catalyzing polyaromatic coke formation.[74,75] Future work should focus on
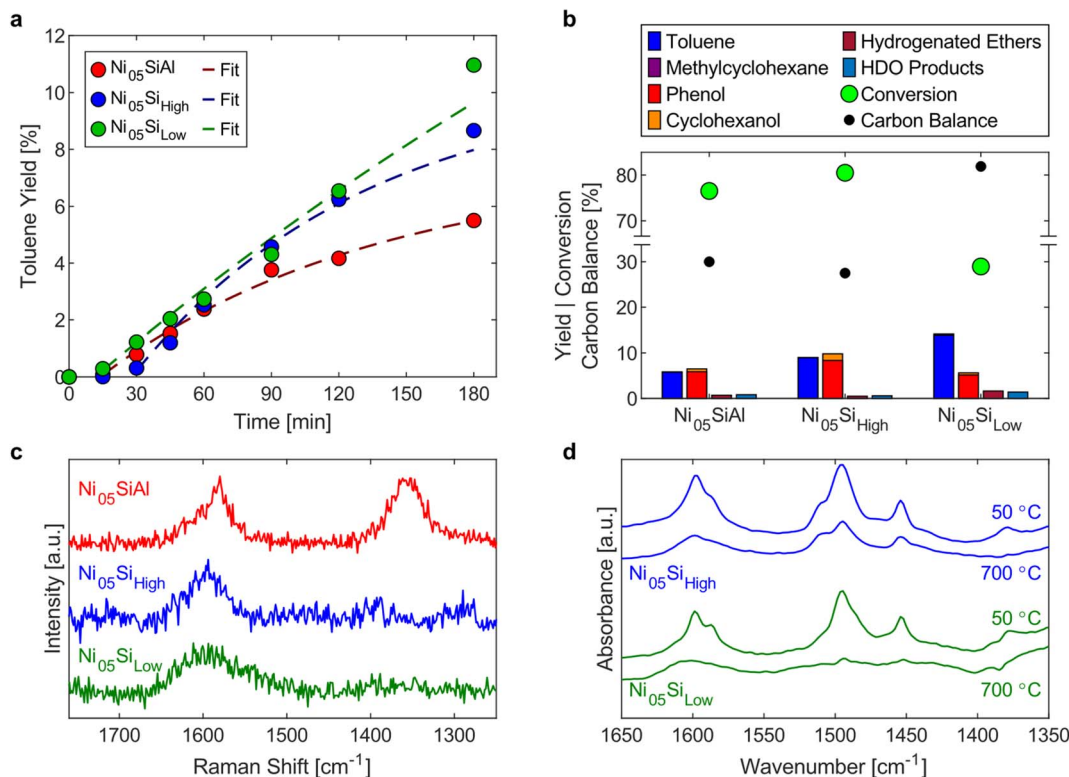
Fig. 5 (a) Toluene yields during the hydrogenolysis of BPE with $Ni_{05}SiAl$ (red), $Ni_{05}Si_{high}$ (blue), and $Ni_{05}Si_{low}$ (green). Fits from the kinetic model are overlaid with the toluene yields. (b) Full product yields, conversion of BPE, and carbon balance after the hydrogenolysis reaction of BPE with $Ni_{05}SiAl$, $Ni_{05}Si_{high}$, and $Ni_{05}Si_{low}$. 1.00 g catalyst, 0.20 g BPE, 25 mL S. S. vessel, 2×15 mm S. S. grinding balls, 20 Hz, 30 sccm H_2. (c) Raman spectra of the spent $Ni_{05}SiAl$ (red), $Ni_{05}Si_{high}$ (blue), and $Ni_{05}Si_{low}$ (green). (d) DRIFTS spectra of the spent $Ni_{05}Si_{high}$ (blue) and $Ni_{05}Si_{low}$ (green) at 50 °C (top) and 700 °C (bottom).

mitigating these side-reactions by optimizing milling intensity and developing supports that are less prone to rupture. Softer material, like activated carbon, should flex and bend under the mechanical impact, and harder material, like zirconium oxide, should be more resilient to rupture.

Conclusions

The mechanocatalytic hydrogenolysis of benzyl phenyl ether, a model lignin ether, was demonstrated using cost-effective, abundant catalysts under ambient H_2 pressure, at room temperature, and without a solvent. The observed reaction network closely matches that for thermal hydrogenolysis of BPE, suggesting similar reactions can be expected to occur between mechanocatalytic and thermocatalytic reactions over metal catalysts. Milling not only supplied the mechanical energy to drive the reaction, but also provided metallic nickel surfaces *in situ*, avoiding the need for high temperature activation steps. Adsorption of phenolic species on mechanically activated domains of the catalyst support was identified as a major source for carbon loss, which provided guidance for the design of more robust mechanocatalysts. Overall, this works demonstrates the underlying chemistry necessary for developing a pathway for mild lignin depolymerization which may be able to avoid many of the safety, technical, and economic issues

hindering the realization of lignin valorization at industrial scales.

Author contributions

C. S. conceptualized and supervised the research. A. W. T. and E. V. P. performed mechanocatalytic reactions. K. L. H. performed catalyst characterization. S. N. and J. X. K. performed DRIFTS experiments. A. W. T. drafted the manuscript. All authors provided edits and comments for the manuscript.

Conflicts of interest

There are no conflicts to declare.

Acknowledgements

Notes and references

1 H. Luo and M. M. Abu-Omar, in *Encyclopedia of Sustainable Technologies*, ed. M. A. Abraham, Elsevier, Oxford, 2017, DOI: **10.1016/B978-0-12-409548-9.10235-0**, pp. 573–585.

2 W. Boerjan, J. Ralph and M. Baucher, *Annu. Rev. Plant Biol.*, 2003, **54**, 519–546.

3 A. W. Tricker, M. J. Stellato, T. T. Kwok, N. S. Kruyer, Z. Wang, S. Nair, V. M. Thomas, M. J. Realff, A. S. Bommarius and C. Sievers, *ChemSusChem*, 2020, **13**, 4624–4632.

4 W. Schutyser, T. Renders, S. Van den Bosch, S. F. Koelewijn, G. T. Beckham and B. F. Sels, *Chem. Soc. Rev.*, 2018, **47**, 852–908.

5 C. Li, X. Zhao, A. Wang, G. W. Huber and T. Zhang, *Chem. Rev.*, 2015, **115**, 11559–11624.

6 T. Renders, G. Van den Bossche, T. Vangeel, K. Van Aelst and B. Sels, *Curr. Opin. Biotechnol.*, 2019, **56**, 193–201.

7 E. Cooreman, T. Vangeel, K. Van Aelst, J. Van Aelst, J. Lauwaert, J. W. Thybaut, S. Van den Bosch and B. F. Sels, *Ind. Eng. Chem. Res.*, 2020, **59**, 17035–17045.

8 K. J. Ardila-Fierro and J. G. Hernández, *ChemSusChem*, 2021, **14**, 2145–2162.

9 S. L. James, C. J. Adams, C. Bolm, D. Braga, P. Collier, T. Friščić, F. Grepioni, K. D. Harris, G. Hyett, W. Jones, A. Krebs, J. Mack, L. Maini, A. G. Orpen, I. P. Parkin, W. C. Shearouse, J. W. Steed and D. C. Waddell, *Chem. Soc. Rev.*, 2012, **41**, 413–447.

10 S. Mateti, M. Mathesh, Z. Liu, T. Tao, T. Ramireddy, A. M. Glushenkov, W. Yang and Y. I. Chen, *Chem. Commun.*, 2021, **57**, 1080–1092.

11 T. Friscic and W. Jones, *Cryst. Growth Des.*, 2009, **9**, 1621–1637.

12 C. Suryanarayana, *Prog. Mater. Sci.*, 2001, **46**, 1–184.

13 A. W. Tricker, G. Samaras, K. L. Hebisch, M. J. Realff and C. Sievers, *Chem. Eng. J.*, 2020, **382**, 122954.

14 S. Amirjalayer, H. Fuchs and D. Marx, *Angew. Chem., Int. Ed.*, 2019, **58**, 5232–5235.

15 S. Immohr, M. Felderhoff, C. Weidenthaler and F. Schüth, *Angew. Chem., Int. Ed.*, 2013, **52**, 12688–12691.

16 A. W. Tricker, K. L. Hebisch, M. Buchmann, Y.-H. Liu, M. Rose, E. Stavitski, A. J. Medford, M. C. Hatzell and C. Sievers, *ACS Energy Lett.*, 2020, **5**, 3362–3367.

17 Z. Liu, J. Liu, S. Mateti, C. Zhang, Y. Zhang, L. Chen, J. Wang, H. Wang, E. H. Doeven and P. S. Francis, *ACS Nano*, 2019, **13**, 1394–1402.

18 D. Tan, L. Loots and T. Friščić, *Chem. Commun.*, 2016, **52**, 7760–7781.

19 B. Szczęśniak, S. Borysiuk, J. Choma and M. Jaroniec, *Mater. Horiz.*, 2020, **7**, 1457–1473.

20 V. Štrukil, *ChemSusChem*, 2021, **14**, 330–338.

21 A. W. Tricker, A. A. Osibo, Y. Chang, J. X. Kang, A. Ganesan, E. Anglou, F. Boukouvala, S. Nair, C. W. Jones and C. Sievers, *ACS Sustainable Chem. Eng.*, 2022, **10**, 11338–11347.

22 M. Baláž, *Environmental Mechanochemistry: Recycling Waste into Materials Using High-Energy Ball Milling*, Springer Nature, 2021.

23 A. Barakat, C. Mayer-Laigle, A. Solhy, R. A. Arancon, H. De Vries and R. Luque, *RSC Adv.*, 2014, **4**, 48109–48127.

24 S. Kuga and M. Wu, *Cellulose*, 2019, **26**, 215–225.

25 Q. Zhang and F. Jerome, *ChemSusChem*, 2013, **6**, 2042–2044.

26 F. Jerome, G. Chatel and K. D. Vigier, *Green Chem.*, 2016, **18**, 3903–3913.

27 M. Kaldstrom, N. Meine, C. Fares, R. Rinaldi and F. Schuth, *Green Chem.*, 2014, **16**, 2454–2462.

28 F. Schuth, R. Rinaldi, N. Meine, M. Kaldstrom, J. Hilgert and M. D. K. Rechulski, *Catal. Today*, 2014, **234**, 24–30.

29 M. D. K. Rechulski, M. Kaldstrom, U. Richter, F. Schuth and R. Rinaldi, *Ind. Eng. Chem. Res.*, 2015, **54**, 4581–4592.

30 D. Y. Lee and M. Sumimoto, *Holzforschung*, 1990, **44**, 347–350.

31 Z. H. Wu, M. Matsuoka, D. Y. Lee and M. Sumimoto, *Mokuzai Gakkaishi*, 1991, **37**, 164–171.

32 S. G. Yao, J. K. Mobley, J. Ralph, M. Crocker, S. Parkin, J. P. Selegue and M. S. Meier, *ACS Sustainable Chem. Eng.*, 2018, **6**, 5990–5998.

33 T. Kleine, J. Buendia and C. Bolm, *Green Chem.*, 2013, **15**, 160–166.

34 A. D. Brittain, N. J. Chrisandina, R. E. Cooper, M. Buchanan, J. R. Cort, M. V. Olarte and C. Sievers, *Catal. Today*, 2018, **302**, 180–189.

35 S. Dabral, H. Wotruba, J. G. Hernandez and C. Bolm, *ACS Sustainable Chem. Eng.*, 2018, 3242–3254, DOI: **10.1021/acssuschemeng.7b03418**.

36 G. Heinicke and I. Lischke, *Z. Phys. Chem.*, 1963, **3**, 355–356.

37 C. Bolm and J. G. Hernandez, *Angew. Chem., Int. Ed.*, 2019, **58**, 3285–3299.

38 S. Mori, W. C. Xu, T. Ishidzuki, N. Ogasawara, J. Imai and K. Kobayashi, *Appl. Catal., A*, 1996, **137**, 255–268.

39 K. Yatagai, Y. Shishido, R. Gemma, T. Boll, H.-H. Uchida and K. Oguri, *Int. J. Hydrogen Energy*, 2020, **45**, 5264–5275.

40 G. Mulas, R. Campesi, S. Garroni, F. Delogu and C. Milanese, *Appl. Surf. Sci.*, 2011, **257**, 8165–8170.

41 Y. Sawama, T. Kawajiri, M. Niikawa, R. Goto, Y. Yabe, T. Takahashi, T. Marumoto, M. Itoh, Y. Kimura and Y. Monguchi, *ChemSusChem*, 2015, **8**, 3773–3776.

42 Y. Sawama, N. Yasukawa, K. Ban, R. Goto, M. Niikawa, Y. Monguchi, M. Itoh and H. Sajiki, *Org. Lett.*, 2018, **20**, 2892–2896.

43 D. J. Nash, D. T. Restrepo, N. S. Parra, K. E. Giesler, R. A. Penabade, M. Aminpour, D. Le, Z. Li, O. K. Farha and J. K. Harper, *ACS Omega*, 2016, **1**, 1343–1354.

44 G.-F. Han, F. Li, Z.-W. Chen, C. Coppex, S.-J. Kim, H.-J. Noh, Z. Fu, Y. Lu, C. V. Singh and S. Siahrostami, *Nat. Nanotechnol.*, 2021, **16**, 325–330.

45 S. Reichle, M. Felderhoff and F. Schüth, *Angew. Chem., Int. Ed.*, 2021, **60**, 26385–26389.

46 A. G. Sergeev and J. F. Hartwig, *Science*, 2011, **332**, 439–443.

47 X. Wang and R. Rinaldi, *ChemSusChem*, 2012, **5**, 1455–1466.

48 D. Wu, Q. Wang, O. V. Safonova, D. V. Peron, W. Zhou, Z. Yan, M. Marinova, A. Y. Khodakov and V. V. Ordomsky, *Angew. Chem., Int. Ed.*, 2021, **60**, 12513–12523.

49 L. Qi, A. Chamas, Z. R. Jones, E. D. Walter, D. W. Hoyt, N. M. Washton and S. L. Scott, *J. Am. Chem. Soc.*, 2019, **141**, 17370–17381.

50 S. Brunauer, P. H. Emmett and E. Teller, *J. Am. Chem. Soc.*, 1938, **60**, 309–319.

51 E. M. v. Duzee and H. Adkins, *J. Am. Chem. Soc.*, 1935, **57**, 147–151.

52 J. He, L. Lu, C. Zhao, D. Mei and J. A. Lercher, *J. Catal.*, 2014, **311**, 41–51.

53 J. He, C. Zhao and J. A. Lercher, *J. Am. Chem. Soc.*, 2012, **134**, 20768–20775.

54 L. Jiang, H. Guo, C. Li, P. Zhou and Z. Zhang, *Chem. Sci.*, 2019, **10**, 4458–4468.

55 R. Parthasarathi, R. A. Romero, A. Redondo and S. Gnanakaran, *J. Phys. Chem. Lett.*, 2011, **2**, 2660–2666.

56 L. Li, H. J. Fan and H. Q. Hu, *Fuel*, 2015, **153**, 70–77.

57 B. Güvenatam, E. H. Heeres, E. A. Pidko and E. J. Hensen, *J. Mol. Catal. A: Chem.*, 2015, **410**, 89–99.

58 B. Guvenatam, O. Kursun, E. H. J. Heeres, E. A. Pidko and E. J. M. Hensen, *Catal. Today*, 2014, **233**, 83–91.

59 C. Espro, B. Gumina, T. Szumelda, E. Paone and F. Mauriello, *Catalysts*, 2018, **8**, 313.

60 F. Mauriello, E. Paone, R. Pietropaolo, A. M. Balu and R. Luque, *ACS Sustainable Chem. Eng.*, 2018, **6**, 9269–9276.

61 A. Sadezky, H. Muckenhuber, H. Grothe, R. Niessner and U. Pöschl, *Carbon*, 2005, **43**, 1731–1742.

62 T. Xing, L. H. Li, L. Hou, X. Hu, S. Zhou, R. Peter, M. Petravic and Y. Chen, *Carbon*, 2013, **57**, 515–519.

63 S. P. Pujari, L. Scheres, A. T. Marcelis and H. Zuilhof, *Angew. Chem., Int. Ed.*, 2014, **53**, 6322–6356.

64 M. J. Stellato, G. Innocenti, A. S. Bommarius and C. Sievers, *Catalysts*, 2021, **11**, 721.

65 S. M. Schimming, O. D. LaMont, M. Konig, A. K. Rogers, A. D. D'Amico, M. M. Yung and C. Sievers, *ChemSusChem*, 2015, **8**, 2073–2083.

66 T. Prasomsri, T. Nimmanwudipong and Y. Román-Leshkov, *Energy Environ. Sci.*, 2013, **6**, 1732–1738.

67 M. Kessler and R. Rinaldi, *Front. Chem.*, 2022, 1099, DOI: **10.3389/fchem.2021.816553**.

68 U. P. Agarwal, J. D. McSweeny and S. A. Ralph, *J. Wood Chem. Technol.*, 2011, **31**, 324–344.

69 F. Madzharova, Z. Heiner and J. Kneipp, *J. Phys. Chem. C*, 2020, **124**, 6233–6241.

70 G. S. Foo, A. K. Rogers, M. M. Yung and C. Sievers, *ACS Catal.*, 2016, **6**, 1292–1307.

71 F. Delogu, *J. Phys. Chem. C*, 2011, **115**, 21230–21235.

72 F. Delogu, *Int. J. Hydrogen Energy*, 2011, **36**, 15145–15152.

73 G. Innocenti, D. J. Benkeser, J. E. Dase, X. Wirth, C. Sievers and K. E. Kurtis, *Fuel*, 2021, **299**, 120892.

74 D. M. Bibby, R. F. Howe and G. D. McLellan, *Appl. Catal., A*, 1992, **93**, 1–34.

75 M. Guisnet and P. Magnoux, *Appl. Catal., A*, 2001, **212**, 83–96.